Geophysical Research Letters

Low Melting Temperature of Anhydrous Mantle Materials at the Core-Mantle Boundary

Taehyun Kim[1] , **Byeongkwan Ko[2]** , **Eran Greenberg[3]** , **Vitali Prakapenka[3]** , **Sang-Heon Shim[2]** , **and Yongjae Lee[1]**

[1]Department of Earth System Sciences, Yonsei University, Seoul, South Korea, [2]School of Earth and Space Exploration, Arizona State University, Tempe, AZ, USA, [3]Center for Advanced Radiation Sources, University of Chicago, Argonne, IL, USA

Abstract One of the central challenges in accurately estimating the mantle melting temperature is the sensitivity of the probe for detecting a small amount of melt at the solidus. To address this, we used a multichannel collimator to enhance the diffuse X-ray scattering from a small amount of melt and probed an eutectic pyrolitic composition to increase the amount of melt at the solidus. Our in situ detection of diffuse scattering from the pyrolitic melt determined an anhydrous melting temperature of 3,302 ± 100 K at 119 ± 6 GPa and 3,430 ± 130 K at the core-mantle boundary (CMB) conditions, as the upper bound temperature. Our CMB temperature is approximately 700 K lower than the previous estimates, implying much faster secular cooling and higher concentrations of S, C, O, and/or H in the region, and nonlinear, advocating the basal magma ocean hypothesis.

Plain Language Summary The heat stored in the Earth's deep interior has been the primary fuel for a range of global processes from mantle convection to surface tectonics, but quantitative estimation of the heat remains uncertain. The melting temperature of mantle materials is one of the key parameters to understanding the thermal evolution and present-day state of the Earth's interior, but it has been poorly constrained, with recent measurement discrepancies as large as 600 K. Here, we report melting temperatures of mantle compositions measured over a wide range of pressures expected for the lower mantle. We investigated a eutectic mantle composition using multichannel collimator filtered X-ray diffraction in combination with the laser-heated diamond-anvil cell. Fitting our melting data over the range of 46–145 GPa led to a solidus temperature of 3,430 ± 130 K at the core-mantle boundary. This temperature is approximately 700 K lower than the previous estimates, implying much faster secular cooling at the lower mantle than previously believed. Furthermore, our solidus curve constrained for a wide pressure range is strongly nonlinear and thus supports the basal magma ocean hypothesis.

1. Introduction

The differentiation and crystallization of the magma ocean, which occurred in the first few million years of the Earth's history, defined the beginnings of the chemical and thermal evolution of our planet (Carlson et al., 2014). Such melting-induced differentiation continues in the deep mantle, albeit regionally, which could be one of the answers for the origin of the present ultra-low velocity zones (ULVZs) at the core-mantle boundary (CMB) (Lay et al., 1998; Wen & Helmberger, 1998; Williams & Garnero, 1996). A prerequisite to understanding such processes is obtaining accurate melting temperatures of silicate mantle materials and their pressure-dependent changes (Labrosse et al., 2007; Stixrude et al., 2009). As the lower mantle is predominantly in solid state in the contemporary Earth (Kennett et al., 1995), the solidus temperature measured from laboratory experiments can also provide an upper bound for the lower-mantle geotherm.

Recently, Fiquet et al. (2010) reported direct detection of diffuse X-ray scattering from partial melt in peridotite at the pressures expected for the CMB in a laser-heated diamond-anvil cell (LHDAC) and estimated a solidus temperature of 4,180 ± 150 K. Subsequently, Andrault et al. (2011) inferred a similar solidus temperature for a chondritic composition at the CMB based on the combination of plateau in the temperature-laser power and rapid recrystallization signatures in diffraction images. Most recently, Nomura et al. (2014) reported a significantly lower solidus temperature of 3,570 ± 200 K at the CMB through X-ray computed tomography as diagnostics for the degree of melting using the temperature quenched samples. Another important
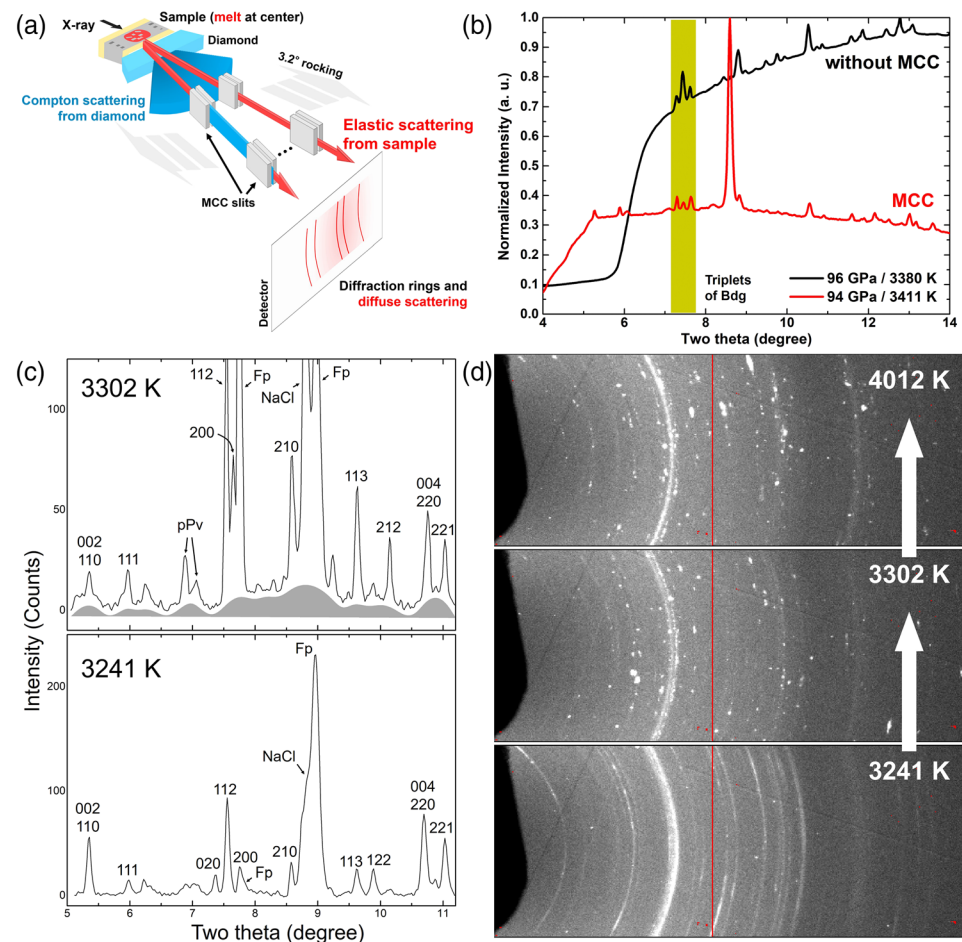
Figure 1. X-ray diffraction setup and melting of estimated eutectic composition of the pyrolitic mantle. (a) A schematic diagram of the experimental setup with MCC. Diffracted X-ray beams from the sample (red arrows) at the rotation center of MCC pass the inner and outer slits of MCC while most of the scattered X-ray beams from anvils (blue fan with gradient) are suppressed by MCC. (b) XRD patterns with (red) and without (black) the MCC setup. (c) Two representative diffraction patterns at 119 GPa showing the growth of diffuse scattering (gray shaded area in the above pattern) upon laser heating from 3,241 K. Peak identifications: *hkl* for bridgmanite, pPv: post-perovskite, Fp: ferropericlase, and NaCl: NaCl pressure medium. (d) Two-dimensional diffraction images of the patterns presented in (c). The red colored lines are the gaps between the modules in the detector.

discrepancy to resolve is the pressure-dependent changes in melting temperature. While Fiquet et al. (2010) found that the rate of increase in solidus temperature decreased strongly with pressure, Andrault et al. (2011) and Nomura et al. (2014) reported a linear pressure dependence of the solidus temperature. This linear solidus (Andrault et al., 2011; Nomura et al., 2014) could lead to the bottom-up crystallization at the lower mantle. However, linear solidus is not consistent with previous theoretical studies (Mosenfelder et al., 2009; Stixrude et al., 2009), which suggested highly curved solidus, leading to lowering the solidus at the CMB conditions, hence supporting the middle-up-down crystallization of magma ocean.

The observed discrepancies arise, at least partly, from the difficulties of objectively detecting melting in high-pressure experiments. Although X-ray diffraction (XRD) can provide an objective melt diagnostic by detecting diffuse scattering from amorphous structure of melt, the diffraction patterns measured from the samples in LHDAC are often dominated by an intense background from the Compton scattering by the diamond anvils, which are thicker than the samples by a factor of at least 200 (Figures 1a and 1b; see Method). These measurements in an XRD experiment require a large amount of melt for reliable melt detection. In addition, if the sample composition is sufficiently different from its eutectic composition, only a small amount of partial melt would form at the onset of the melting temperature. To produce enough melt to be

detected in diffraction pattern, samples must be heated to temperatures sufficiently higher over the solidus temperature. Thus, the solidus temperature is often overestimated. This problem could worsen for silicates because of their small X-ray scattering cross section. Electron microscopy (Fiquet et al., 2010) or X-ray imaging (Nomura et al., 2014) of the recovered samples may be advantageous in detecting a small amount of melt, but these methods can produce ambiguous results because they are usually conducted for the recovered samples at 1 bar. Thus, the sample may have undergone textural changes during decompression, which can obscure identification of the exact location where the temperature was measured at high pressures.

Volatiles contained in the starting materials may also contribute to the existing discrepancy. The experiments on glass-starting materials synthesized through high-temperature melting (and therefore presumed to be anhydrous) resulted in systematically higher solidus temperatures (Andrault et al., 2011; Fiquet et al., 2010). On the other hand, the starting material used by Nomura et al. (2014), a gel with ~400 ppm of H_2O, may have been a reason for their low solidus temperature (Fiquet, 2018). Although H_2O can reduce melting temperature, multi-anvil experiments (Litasov et al., 2001) found that as much as 2 wt% H_2O decreases the solidus temperature of pyrolite only by 180–240 K at 24 GPa. These findings raise an important question whether the 400 ppm H_2O in Nomura et al. (2014) could reduce the solidus temperature by approximately 600 K to explain the discrepancy.

Here, we report a new melting curve of pyrolitic composition by taking advantage of (1) near eutectic model composition and (2) multichannel collimator (MCC)-filtered XRD. This enabled us to detect a small amount of melt at the CMB conditions establishing our solidus temperature the lowest thus far reported on anhydrous mantle materials by as much as 700 K. For direct comparison with previous results, we used glass-starting materials synthesized from the laser levitation method (Tangeman et al., 2001), which are essentially the same as those used by Fiquet et al. (2010) and Andrault et al. (2011).

2. Results

We made important technical improvements in the measurement of the solidus temperatures of silicates in LHDAC by addressing some major issues discussed above. First, we employed a MCC to filter the background Compton scattering from diamond anvils (and cBN seat) to enhance detection of diffuse scattering from a small amount of melt, which has never been attempted for silicate melts at high pressure to our knowledge. The significance of this improvement is that we determine melting point based on an objective criterion. Second, we studied the predicted anhydrous eutectic composition as well as anhydrous pyrolitic (McDonough & Sun, 1995) composition in MgO-FeO-SiO_2 (hereafter Eu-MFS; see supporting information Table S1 and Method). The Eu-MFS sample is important for the accurate determination of solidus temperature, because an ideal eutectic composition would undergo complete melting without a mixed phase region of solid and liquid, providing maximum contrast in scattering properties across the melting point (Baron et al., 2017). We note that the existing studies are not in complete agreement on the eutectic composition at the lower-mantle conditions (de Koker et al., 2013; Ozawa et al., 2018). Even if the exact eutectic composition is not clearly known, the larger amount of melt generated from a near-eutectic composition would still improve the accuracy of melt detection because of the expected large production of melt at the solidus. Lastly, we conducted ex situ transmission electron microscopy (TEM) to further confirm the melting signatures from the recovered sample, providing independent constraints for melting.

2.1. Determination of Solidus Temperature

At 119 GPa, we synthesized stable mantle crystalline phases by heating the Eu-MFS glass to 2,000–2,500 K. We observed the diffraction lines of bridgmanite, post-perovskite, and ferropericlase during heating. Laser heating for melting was then performed for these pretransformed spots. Upon heating the crystalline mixture above 3,302 ± 100 K at 119 GPa, diffraction patterns revealed a clear diffuse scattering signal, suggesting the appearance of a phase without long-range ordering, that is, melt (Figure 1c). The diffuse scattering intensified with further heating, up to 4,012 ± 158 K. The intensity gain was more pronounced at temperatures between 3,241 and 3,302 K than between 3,302 and 4,012 K, suggesting that the solidus temperature of Eu-MFS is within the former temperature range. In principle, all the diffraction lines from crystalline phases should disappear across a solidus at eutectic composition. The fact that we still observed diffraction lines from crystalline phases may indicate that our composition was somewhat different from the true eutectic composition at this pressure range. In addition, although the size of the heating
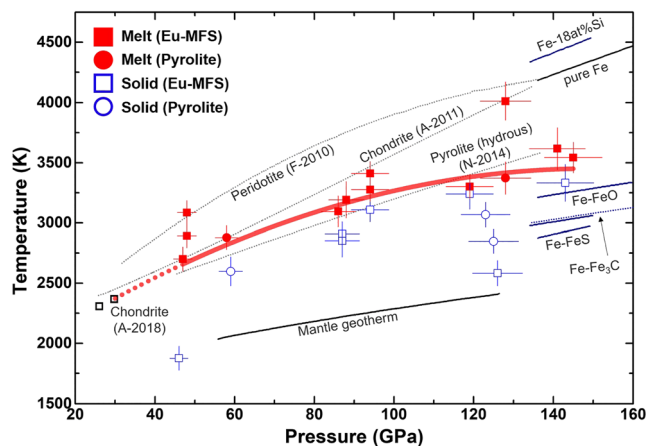
Figure 2. Solidus temperatures of mantle materials. The solid and open symbols represent observations of partial melting and no melting in our experiments, respectively. The circles and squares indicate pyrolite and Eu-MFS results, respectively. The error bars in temperature and pressure are estimated to be 1σ uncertainties. We plot the mantle geotherm (Brown & Shankland, 1981) and solidi from previous reports (F-2010, Fiquet et al., 2010; A-2011, Andrault et al., 2011; N-2014, Nomura et al., 2014; and A-2018, Andrault et al., 2018) for comparison. The melting temperatures of pure Fe (Anzellini et al., 2013), Fe-FeO, Fe-FeS, Fe-Fe$_3$C, Fe-18at%Si (continuous lines, Morard et al., 2017), and Fe-Fe$_3$C (dotted line, Mashino et al., 2019) are also plotted.

spot (20 microns in diameter) was much greater than that of the X-ray beam (3 microns in diameter), diffraction from the lower-temperature part of the heating spot (likely the edge of the hot spot) may have contributed to the intensities of the measured diffraction lines.

Concurrently with the appearance of diffuse scattering, we observed significant changes in the diffraction images (Figure 1d). Above 3,302 K, the diffraction rings became spotty, and the spots migrated into different azimuthal angles with progression of heating. Similar changes in diffraction images have been documented in previous experiments and were attributed to rapid recrystallization from silicate melt (Andrault et al., 2011). We note, however, that melting is not the sole source of recrystallization. For example, in the case of metallic iron, recrystallization features in the diffraction images appeared before melting (Anzellini et al., 2013). Nonetheless, the fact that the diffraction spots moved concurrently with the growth of diffuse scattering in our experiment confirms that, in the case of silicates, such changes are related to melt formation.

In heating runs at lower pressures, diffuse scattering features (between 7.5° and 9.5° in 2θ in Figure 1c) became less clear (see the red arrow in Figure S2) because of the overlap with diffraction peaks from NaCl, which was used as thermal insulation layers. This observation could also mean that our Eu-MFS composition was closer to the eutectic point at higher pressure range (i.e., near 119 GPa). We also observed the appearance of diffuse scattering (near 8° in 2θ in Figure S7) at 94 GPa and 3,214 K and 96 GPa and 3,389 K for a sample without a NaCl insulator and MCC setup.

In the case of the pyrolite samples, the detection of diffuse scattering was more difficult because it generated a smaller amount of melt at the solidus than Eu-MFS. On the other hand, the changes in the diffraction rings remain a clear indicator for melting (Figures S3 and S4).

Between 40 and 80 GPa, our solidus temperatures of anhydrous pyrolite and Eu-MFS were in good agreement (i.e., within ±150 K) with those reported for anhydrous chondrite by Andrault et al. (2011) and for pyrolite with 400 ppm H_2O by Nomura et al. (2014) (Figure 2 and Table S2). At this pressure range, however, the solidus temperatures reported by Fiquet et al. (2010) for anhydrous pyrolite were 400–600 K higher than both our and other studies. In Fiquet et al. (2010), the detection of diffuse scattering was reported at 3750 K and 61 GPa, which is close to the liquidus temperature at that pressure in our study. Our solidus temperatures, together with those of Andrault et al. (2011) and Nomura et al. (2014), were also in better agreement with the recent multi-anvil result (Andrault et al., 2018) on a chondritic composition up to 28 GPa, where a small amount of melt was detected in electrical conductivity measurement for an accurate determination of the melting temperature.

Above 80 GPa, the pressure-dependent increase in our solidus temperature was progressively reduced compared to the linear increase suggested by Andrault et al. (2011) and crossed the linear solidus reported by Nomura et al. (2014) (within ±150 K). The chondritic composition in Andrault et al. (2011) had a 0.44 mole fraction of SiO_2, X (SiO_2), substantially higher than that of pyrolite (0.33). Both theoretical and experimental studies (de Koker et al., 2013; Ozawa et al., 2018) have shown that the eutectic X (SiO_2) value decreases from 0.4–0.42 to 0.3–0.38 with an increase in pressure from 25 to 136 GPa. Therefore, while the X (SiO_2) value of the chondritic composition is close to that of the eutectic composition at low pressures, the difference from eutectic composition would increase with pressure due to the decrease in eutectic X (SiO_2). Such an increased difference in X (SiO_2) in the higher pressure regime for the chondritic composition used by Andrault et al. (2011) would generate a progressively smaller amount of partial melt at the solidus temperature (from approximately 80 vol.% to less than 50 vol.%; Figure S5). In addition, because the melting criteria (i.e., combination of plateau in the temperature-laser power and rapid recrystallization) employed by Andrault et al. (2011) would require a certain amount of melt for detection, the increasing compositional difference would require a progressively higher degree of partial melting. Therefore, the magnitude of the overestimation in the solidus temperatures would increase as a
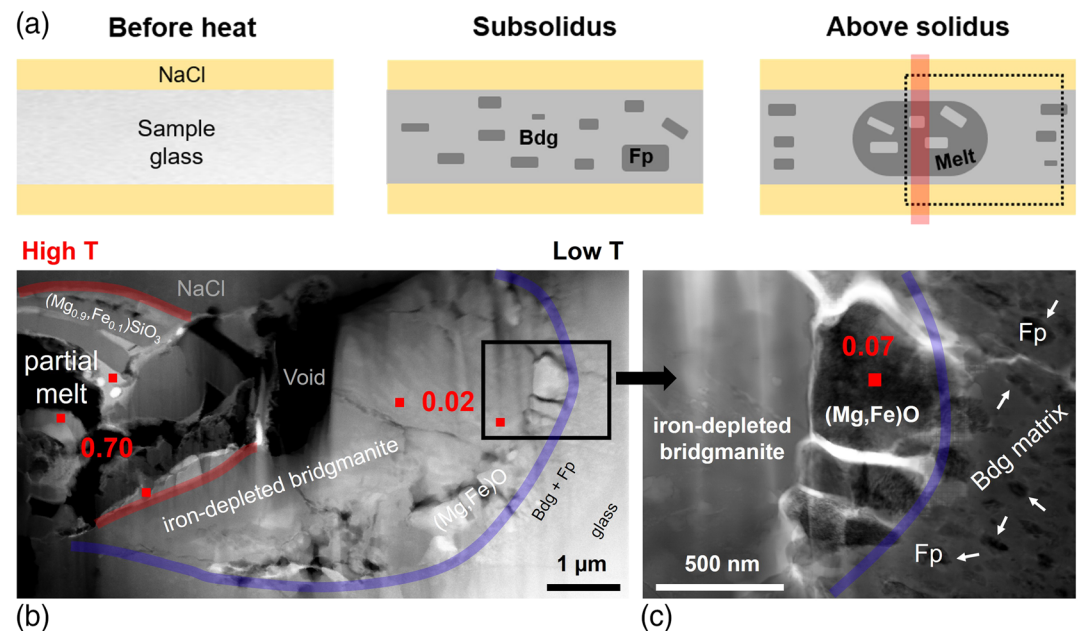
Figure 3. TEM images of a laser-heated spot in Eu-MFS at 94 GPa and 3,411 K. (a) Schematic diagram of textural changes during laser heating as inferred from our TEM observations. The X-ray position (a width of 3 μm) is indicated by the red vertical (thick) line. (b) A molten spot (left side) surrounded by a lower temperature area (toward the right side) with iron-depleted bridgmanite. The numbers in red indicate Fe/(Mg + Fe) in mole at the positions by red squares. This image corresponds to the dotted rectangle in (a). (c) A magnified area of the black rectangle in (b). The edge of the heated spot is mostly composed of materials close to (Mg,Fe)O, which we interpret as frozen partial melt mobilized along the thermal gradient and crystallized. The area at the right side of the blue curve shows ferropericlase grains (some grains are pointed by white arrows) in bridgmanite matrix, which is typical for the region without melting.

function of pressure, possibly leading to the unusual linear shape of the solidus curve (Andrault et al., 2011).

The projected solidus temperature at the CMB is $3,430 \pm 130$ K for both Eu-MFS and pyrolitic samples. This solidus temperature at the CMB condition was similar to that estimated for pyrolite, with 400 ppm H_2O in Nomura et al. (2014) (e.g., $3,570 \pm 200$ K at 136 GPa). Again, our starting glass samples were synthesized and handled the same way as in Fiquet et al. (2010) and Andrault et al. (2011), where the samples were perceived to be anhydrous. As mentioned above, the multi-anvil study found that 2 wt% H_2O can reduce the solidus temperature by 180–240 K at 24 GPa (Litasov et al., 2001). If we assume a linear depression effect of H_2O on solidus temperature, 400 ppm (0.04 wt%) H_2O (Nomura et al., 2014) would reduce the solidus temperature only by 5 K, which is beyond the resolution of melting experiments in LHDAC. Although an enhanced effect of H_2O cannot be ruled out at higher pressures, the low solidus temperature of pyrolite in 400 ppm H_2O and our new results showed that the effect of H_2O would not explain the observed discrepancies in solidus temperature of similar mantle compositions.

2.2. Chemical and Textural Analysis of Melting Spots

To further confirm the existence of partial melt in the samples measured in our in situ XRD experiments, we conducted textural and compositional analysis using TEM for three recovered samples (Figures 3 and S4 and Table S3), which fit to the following conditions: coaxial alignment of the X-ray and laser positions during and after heating, partial melting signatures such as diffuse X-ray scattering, and recrystallization during partial melting. The hot spot and adjacent area were sectioned via the focused ion beam (FIB) method. The cross section of the heated spot in the Eu-MFS sample recovered from 94 GPa showed characteristic melting textures similar to those reported in the previous studies (Figure 3a) (Andrault et al., 2011; Fiquet et al., 2010). The center of the heated spot (high *T* area and inner region of the red lines in Figure 3b), which we interpreted as frozen melt, contained more Fe and less Si than the starting composition.

In the surrounding area (low T area at the region between the red and the blue lines in Figure 3b) of the frozen melt, Fe-depleted bridgmanite was identified. The same texture was also observed in the previous studies (Andrault et al., 2011; Nomura et al., 2014; Tateno et al., 2014). Near the edge of solid (Fe-depleted bridgmanite in Figure 3c), we found a small amount of Fe-rich and Si-deficient grains with a composition very close to that of ferropericlase, which we interpret as migrated partial melt to cold region. In fact, we observed that the ferropericlase diffraction lines became progressively weaker with heating above solidus at pressures above 46 GPa, suggesting that the removed (Mg,Fe)O component went into melt. Our interpretation is also consistent with previous observations (Tateno et al., 2014). On the other hand, the region outside of the blue line in the Eu-MFS sample is characterized by ferropericlase crystals embedded in the bridgmanite matrix with a volume ratio expected for the composition of the starting glass material, suggesting that the area did not experience melting (Piet et al., 2016). Our TEM observation of a pyrolite sample recovered from 58 GPa showed similar textural features related to melting (Figure S4). However, the melting structure was smaller than those found in our Eu-MFS sample, likely because pyrolitic composition is away from the eutectic point (Figure S5).

Our chemical analyses confirmed much higher Fe content in the spots we interpreted as molten structure (Figure 3b), consistent with previous studies (Andrault et al., 2012; Nomura et al., 2011; Tateno et al., 2014) in which Fe preferentially partitioned into melt over crystalline residue. From this, we estimated Fe-Mg partition coefficients between the crystalline phases and the melt (K_D), $K_D = ([\text{Fe}^{\text{solid}}]/[\text{Mg}^{\text{solid}}])/([\text{Fe}^{\text{melt}}]/[\text{Mg}^{\text{melt}}])$. For the pyrolite sample, we obtained $K_D = 0.260$ at 58 GPa (Figure S6 and Table S3), which is in excellent agreement with the previously reported value (Tateno et al., 2014). The Eu-MFS sample exhibited much lower K_D values (0.0131 and 0.0024 at 94 and 145 GPa, respectively; Figure S6). We attribute the lower value to the absence of Al content in the Eu-MFS composition. In conclusion, both the textural and chemical signatures from our TEM measurements support our in situ XRD melting observations.

3. Discussion

3.1. Lower Temperature for the CMB

The solidus temperature at the CMB we reported here (e.g., 3,430 ± 130 K) is substantially lower than those reported thus far for the anhydrous mantle compositions (e.g., 4,150 and 4,180 K) (Andrault et al., 2011; Fiquet et al., 2010). Current seismic studies (Yu & Garnero, 2018) indicate no global melting at any depth ranges in the lower mantle, only some localized partial melt structures at the lowermost mantle (such as ULVZs). Therefore, our solidus temperature would place the upper bound for the contemporary mantle geotherm. Furthermore, currently established models of secular cooling have predicted a much higher temperature at the CMB than demonstrated by our study (Andrault et al., 2017). The low CMB temperature we constrained from our melting experiments would thus require these models to be revised to reflect a much faster rate of cooling for the mantle than previously believed. This implies that the early lower mantle and the core had to cool down with higher thermal conductivities (Manthilake et al., 2011; Ohta et al., 2016; Stackhouse et al., 2015), although these values are under debate (Geballe et al., 2020; Konôpková et al., 2016). The consideration of higher thermal conductivities in the lower mantle and the core would require another energy source (e.g., thermochemical convection) or higher temperature at the CMB (higher than 7,000 K, 4.5 Gy ago) (Labrosse, 2014) to sustain geodynamo from at least 3.5 Gy ago. Recently, the exsolution of certain mantle components has been suggested to contribute to sustaining geodynamo by composition-driven convection (Badro et al., 2016; O'Rourke & Stevenson, 2016). Consequently, our result would favor such a scenario that the Earth may have cooled faster than what we have expected (Olson, 2013).

3.2. Relationship Between the Low Melting Temperature of Pyrolite and the Outer Core Composition

The temperature offset across the CMB is expected to be small (Lay et al., 2008); therefore, our lower solidus required for the CMB implies that the outermost outer core is cooler than what we have thought, which is also important in understanding the thermal and chemical states of the outer core. When combined with the melting data for metallic iron and iron alloys, our results provide new insights into the light element contents in the molten outer core. Because the difference between the melting temperature of pure metallic iron (i.e., 4,050 ± 500 K, Anzellini et al., 2013, or 3,760 ± 290 K, Sinmyo et al., 2019) and the solidus temperature we report here, 3,430 ± 130 K, is larger than previously estimated, higher concentrations of light elements
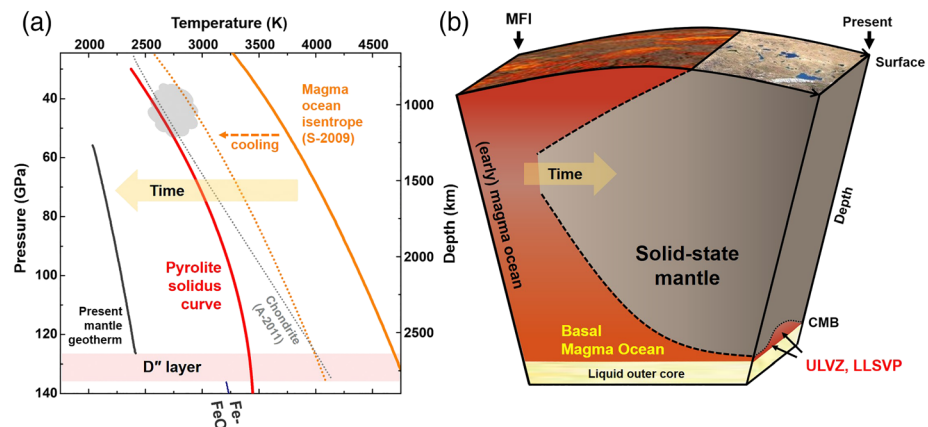
Figure 4. The schematic diagram for the thermal evolution of the mantle (not to scale). (a) Showing the magma ocean isentrope intersections with the two different solidus curves. Upon cooling of the magma ocean and changes in its isentrope curvature (Stixrude et al., 2009) crystallization would occur from the mid-mantle when the magma ocean geotherm intersected with the curved solidus of the mantle as determined by our study (red continuous line). This model would leave the lowermost mantle partially molten until much later stages in the Earth's thermal evolution. On the other hand, linear solidus from previous study (black dotted line) (Andrault et al., 2011) would favor bottom-up crystallization. (b) Secular changes of the mantle from the Moon-forming impact (MFI) to the present day. After MFI, the magma ocean underwent cooling (Stixrude et al., 2009). The ULVZs may be the remnant basal magma ocean supported by our study. Our results together with previous reports (Nomura et al., 2014) suggest Fe-rich composition for the ULVZs. LLSVPs could also be related to the basal magma ocean model (Labrosse et al., 2007).

would be required to sufficiently depress the melting temperature of iron, at least in the upper part of the outer core. Si is known to have a marginal effect on (or even to increase) the melting temperature of metallic iron (Fischer et al., 2013). In contrast, S, C, O, and H are more efficient in lowering the melting temperature of iron at the CMB (Mashino et al., 2019; Morard et al., 2017), even with smaller concentrations. Based on the higher solidus temperature of silicates reported earlier (Andrault et al., 2011; Fiquet et al., 2010), Morard et al. (2017) proposed that at least 2 wt% of C or S or 5 wt% of O is contained in the outer core to fit the mantle solidus at the CMB.

Our results showed that anhydrous pyrolitic materials melt at a temperature lower by approximately 700 K, compared to the temperature adopted by Morard et al. (2017). Our lower solidus temperature thus requires higher concentration of these light elements in the outer core: at minimum, 4 wt% C or S or 10 wt% O, if we extrapolate on the basis of a linear increase of light element concentration for melting temperature depression. These amounts of light elements are still within the density deficit discussed in the literature for the outer core (Hirose et al., 2017). Our lower CMB temperature would also limit the amount of Si as a light element in the outer core, as it would not lower the solidus temperature sufficiently to maintain the liquid state of the region.

3.3. Origin of the Fe-Enriched Provinces at the CMB

Another important implication from our results can be inferred from the shape of the measured solidus, which was significantly different from those suggested by Andrault et al. (2011) and Nomura et al. (2014). As discussed above, the linear solidus found in Andrault et al. (2011) could have resulted from the increasing difference from eutectic composition at higher pressures. The linear trend reported by Nomura et al. (2014) might be related to the volatile content and/or the different melt diagnostics. We also note that their data points exist mostly at pressures above 100 GPa, making it difficult to constrain the shape of their solidus.

The controversy over the shape of the solidi has allowed for a range of different models for the crystallization in the magma ocean, from bottom-up freezing (Andrault et al., 2011, 2012) to middle up down freezing (or the basal magma ocean model) (Labrosse et al., 2007; Nomura et al., 2011). Therefore, the strong curvature found in our study can narrow the possible models for the early evolution of the Earth's mantle (Labrosse et al., 2007; Mosenfelder et al., 2009; Stixrude et al., 2009). As shown in Figure 4, our strongly curved solidus would intersect the isentrope of the cooling magma ocean at the mid-mantle. Based on our

data and the isentrope from Stixrude et al. (2009), we suggest that such complete solidification might have first occurred in the mid-mantle (at the top of the lower-mantle indicated by gray shaded area in Figure 4a). With further cooling, the complete solidification fronts would have progressed both upwards and, to longer extent, downwards.

As such, our solidus curve suggests that the last region remaining from the early magma ocean would be the lowermost mantle. Seismic measurements have shown that ULVZs found at the CMB have unusually low shear velocity, and the ratio between shear and compressional wave speed supports the presence of partial melt in the structures (Yuan & Romanowicz, 2017). Although indirect, seismic constraints also suggest higher density for the ULVZs (Rost et al., 2005). Our TEM analyses revealed partitioning of Fe preferentially into melts over crystalline silicates, consistent with the former studies (Nomura et al., 2014). Furthermore, Fe is known to decrease the melting temperature of mantle silicates (Boukaré et al., 2015; Deng et al., 2019; Fu et al., 2018). Therefore, our experiments support the hypothesis that ULVZs might be Fe-rich dense silicates containing partial melt (Williams & Garnero, 1996) originated from the early magma ocean (Labrosse et al., 2007). However, it is possible that not all the ULVZs were formed from the basal magma ocean (Garnero et al., 2016; Yu & Garnero, 2018), so it is important that future studies investigate regional variations in the properties of ULVZs. The magma ocean model has also been discussed for the large low shear velocity provinces (LLSVPs) found beneath the central Pacific and Africa (Frost & Rost, 2014; Lynner & Long, 2014). While further laboratory measurements such as elastic constants and sound velocities at high P-T are needed for comparison with seismically measured properties of LLSVPs, our strongly curved solidus favors the idea of a partially molten lowermost mantle until a later period of the Earth's thermal history and its possible contribution to the formation of LLSVPs as distinct geochemical reservoirs in the freezing basal magma ocean (Labrosse et al., 2007).

Conflict of Interest

All authors do not have financial conflict of interests.

Data Availability Statement

All X-ray diffraction and TEM-EDS data supporting this study area are freely available at https://zenodo.org/record/3903978#.XvU3pSgzb-h or available by contacting the corresponding author (yongjae-lee@yonsei.ac.kr).

References

Andrault, D., Bolfan-Casanova, N., Bouhifd, M. A., Boujibar, A., Garbarino, G., Manthilake, G., et al. (2017). Toward a coherent model for the melting behavior of the deep Earth's mantle. *Physics of the Earth and Planetary Interiors*, *265*, 67–81. https://doi.org/10.1016/j.pepi.2017.02.009

Andrault, D., Bolfan-Casanova, N., Nigro, G. L., Bouhifd, M. A., Garbarino, G., & Mezouar, M. (2011). Solidus and liquidus profiles of chondritic mantle: Implication for melting of the Earth across its history. *Earth and Planetary Science Letters*, *304*(1–2), 251–259. https://doi.org/10.1016/j.epsl.2011.02.006

Andrault, D., Pesce, G., Manthilake, G., Monteux, J., Bolfan-Casanova, N., Chantel, J., et al. (2018). Deep and persistent melt layer in the Archaean mantle. *Nature Geoscience*, *11*(2), 139–143. https://doi.org/10.1038/s41561-017-0053-9

Andrault, D., Petitgirard, S., Lo Nigro, G., Devidal, J. L., Veronesi, G., Garbarino, G., & Mezouar, M. (2012). Solid-liquid iron partitioning in Earth's deep mantle. *Nature*, *487*(7407), 354–357. https://doi.org/10.1038/nature11294

Anzellini, S., Dewaele, A., Mezouar, M., Loubeyre, P., & Morard, G. (2013). Melting of iron at earth's inner core boundary based on fast X-ray diffraction. *Science*, *340*(6131), 464–466. https://doi.org/10.1126/science.1233514

Badro, J., Siebert, J., & Nimmo, F. (2016). An early geodynamo driven by exsolution of mantle components from Earth's core. *Nature*, *536*(7616), 326–328. https://doi.org/10.1038/nature18594

Baron, M. A., Lord, O. T., Myhill, R., Thomson, A. R., Wang, W., Trønnes, R. G., & Walter, M. J. (2017). Experimental constraints on melting temperatures in the MgO–SiO2 system at lower mantle pressures. *Earth and Planetary Science Letters*, *472*, 186–196. https://doi.org/10.1016/j.epsl.2017.05.020

Boukaré, C. E., Ricard, Y., & Fiquet, G. (2015). Thermodynamics of the MgO-FeO-SiO2 system up to 140 GPa: Application to the crystallization of Earth's magma ocean. *Journal of Geophysical Research: Solid Earth*, *120*, 6085–6101. https://doi.org/10.1002/2015JB011929

Brown, J. M., & Shankland, T. J. (1981). Thermodynamic parameters in the Earth as determined from seismic profiles. *Geophysical Journal of the Royal Astronomical Society*, *66*(3), 579–596. https://doi.org/10.1111/j.1365-246X.1981.tb04891.x

Carlson, R. W., Garnero, E., Harrison, T. M., Li, J., Manga, M., McDonough, W. F., et al. (2014). How did early earth become our modern world? *Annual Review of Earth and Planetary Sciences*, *42*(1), 151–178. https://doi.org/10.1146/annurev-earth-060313-055016

de Koker, N., Karki, B. B., & Stixrude, L. (2013). Thermodynamics of the MgO-SiO2 liquid system in Earth's lowermost mantle from first principles. *Earth and Planetary Science Letters*, *361*, 58–63. https://doi.org/10.1016/j.epsl.2012.11.026

Deng, J., Miyazaki, Y., & Lee, K. K. M. (2019). Implications for the melting phase relations in the MgO-FeO system at core-mantle boundary conditions. *Journal of Geophysical Research: Solid Earth*, *124*, 1294–1304. https://doi.org/10.1029/2018JB015499

Fiquet, G. (2018). Chapter 4—Melting in the Earth's deep interior. In Y. Kono & C. Sanloup (Eds.), *Magmas Under Pressure* (pp. 115–134). New York: Elsevier.

Fiquet, G., Auzende, A. L., Siebert, J., Corgne, A., Bureau, H., Ozawa, H., & Garbarino, G. (2010). Melting of peridotite to 140 gigapascals. *Science*, *329*(5998), 1516–1518. https://doi.org/10.1126/science.1192448

Fischer, R. A., Campbell, A. J., Reaman, D. M., Miller, N. A., Heinz, D. L., Dera, P., & Prakapenka, V. B. (2013). Phase relations in the Fe-FeSi system at high pressures and temperatures. *Earth and Planetary Science Letters*, *373*, 54–64. https://doi.org/10.1016/j.epsl.2013.04.035

Frost, D. A., & Rost, S. (2014). The P-wave boundary of the large-low shear velocity province beneath the Pacific. *Earth and Planetary Science Letters*, *403*, 380–392. https://doi.org/10.1016/j.epsl.2014.06.046

Fu, S., Yang, J., Zhang, Y., Liu, J., Greenberg, E., Prakapenka, V. B., et al. (2018). Melting behavior of the lower-mantle ferropericlase across the spin crossover: Implication for the ultra-low velocity zones at the lowermost mantle. *Earth and Planetary Science Letters*, *503*, 1–9. https://doi.org/10.1016/j.epsl.2018.09.014

Garnero, E. J., McNamara, A. K., & Shim, S. H. (2016). Continent-sized anomalous zones with low seismic velocity at the base of Earth's mantle. *Nature Geoscience*, *9*(7), 481–489. https://doi.org/10.1038/ngeo2733

Geballe, Z. M., Sime, N., Badro, J., van Keken, P. E., & Goncharov, A. F. (2020). Thermal conductivity near the bottom of the Earth's lower mantle: Measurements of pyrolite up to 120 GPa and 2500 K. *Earth and Planetary Science Letters*, *536*, 116161. https://doi.org/10.1016/j.epsl.2020.116161

Hirose, K., Morard, G., Sinmyo, R., Umemoto, K., Hernlund, J., Helffrich, G., & Labrosse, S. (2017). Crystallization of silicon dioxide and compositional evolution of the Earth's core. *Nature*, *543*(7643), 99–102. https://doi.org/10.1038/nature21367

Kennett, B. L. N., Engdahl, E. R., & Buland, R. (1995). Constraints on seismic velocities in the Earth from traveltimes. *Geophysical Journal International*, *122*(1), 108–124. https://doi.org/10.1111/j.1365-246X.1995.tb03540.x

Konôpková, Z., McWilliams, R. S., Gómez-Pérez, N., & Goncharov, A. F. (2016). Direct measurement of thermal conductivity in solid iron at planetary core conditions. *Nature*, *534*(7605), 99–101. https://doi.org/10.1038/nature18009

Labrosse, S. (2014). Thermal evolution of the core with a high thermal conductivity. *Physics of the Earth and Planetary Interiors*, *247*, 36–55.

Labrosse, S., Hernlund, J. W., & Coltice, N. (2007). A crystallizing dense magma ocean at the base of the Earth's mantle. *Nature*, *450*(7171), 866–869. https://doi.org/10.1038/nature06355

Lay, T., Hernlund, J., & Buffett, B. A. (2008). Core-mantle boundary heat flow. *Nature Geoscience*, *1*(1), 25–32. https://doi.org/10.1038/ngeo.2007.44

Lay, T., Williams, Q., & Garnero, E. J. (1998). The core-mantle boundary layer and deep Earth dynamics. *Nature*, *392*(6675), 461–468. https://doi.org/10.1038/33083

Litasov, K., Ohtani, E., & Taniguchi, H. (2001). Melting relations of hydrous pyrolite in CaO-MgO-Al2O3-SiO2-H2O system at the transition zone pressures. *Geophysical Research Letters*, *28*(7), 1303–1306. https://doi.org/10.1029/2000GL012291

Lynner, C., & Long, M. D. (2014). Lowermost mantle anisotropy and deformation along the boundary of the African LLSVP. *Geophysical Research Letters*, *41*, 3447–3454. https://doi.org/10.1002/2014GL059875

Manthilake, G. M., de Koker, N., Frost, D. J., & McCammon, C. A. (2011). Lattice thermal conductivity of lower mantle minerals and heat flux from Earth's core. *Proceedings of the National Academy of Sciences of the United States of America*, *108*(44), 17,901–17,904. https://doi.org/10.1073/pnas.1110594108

Mashino, I., Miozzi, F., Hirose, K., Morard, G., & Sinmyo, R. (2019). Melting experiments on the Fe–C binary system up to 255 GPa: Constraints on the carbon content in the Earth's core. *Earth and Planetary Science Letters*, *515*, 135–144. https://doi.org/10.1016/j.epsl.2019.03.020

McDonough, W. F., & Sun, S. S. (1995). The composition of the Earth. *Chemical Geology*, *120*(3–4), 223–253. https://doi.org/10.1016/0009-2541(94)00140-4

Morard, G., Andrault, D., Antonangeli, D., Nakajima, Y., Auzende, A. L., Boulard, E., et al. (2017). Fe–FeO and Fe–Fe3C melting relations at Earth's core–mantle boundary conditions: Implications for a volatile-rich or oxygen-rich core. *Earth and Planetary Science Letters*, *473*, 94–103. https://doi.org/10.1016/j.epsl.2017.05.024

Mosenfelder, J. L., Asimow, P. D., Frost, D. J., Rubie, D. C., & Ahrens, T. J. (2009). The MgSiO3 system at high pressure: Thermodynamic properties of perovskite, postperovskite, and melt from global inversion of shock and static compression data. *Journal of Geophysical Research*, *114*, B01203. https://doi.org/10.1029/2008JB005900

Nomura, R., Hirose, K., Uesugi, K., Ohishi, Y., Tsuchiyama, A., Miyake, A., & Ueno, Y. (2014). Low core-mantle boundary temperature inferred from the solidus of pyrolite. *Science*, *343*(6170), 522–525. https://doi.org/10.1126/science.1248186

Nomura, R., Ozawa, H., Tateno, S., Hirose, K., Hernlund, J., Muto, S., et al. (2011). Spin crossover and iron-rich silicate melt in the Earth's deep mantle. *Nature*, *473*(7346), 199–202. https://doi.org/10.1038/nature09940

Ohta, K., Kuwayama, Y., Hirose, K., Shimizu, K., & Ohishi, Y. (2016). Experimental determination of the electrical resistivity of iron at Earth's core conditions. *Nature*, *534*(7605), 95–98. https://doi.org/10.1038/nature17957

Olson, P. (2013). The new core paradox. *Science*, *342*(6157), 431–432. https://doi.org/10.1126/science.1243477

O'Rourke, J. G., & Stevenson, D. J. (2016). Powering Earth's dynamo with magnesium precipitation from the core. *Nature*, *529*(7586), 387–389. https://doi.org/10.1038/nature16495

Ozawa, K., Anzai, M., Hirose, K., Sinmyo, R., & Tateno, S. (2018). Experimental determination of eutectic liquid compositions in the MgO-SiO2 system to the lowermost mantle pressures. *Geophysical Research Letters*, *45*, 9552–9558. https://doi.org/10.1029/2018GL079313

Piet, H., Badro, J., Nabiei, F., Dennenwaldt, T., Shim, S. H., Cantoni, M., et al. (2016). Spin and valence dependence of iron partitioning in Earth's deep mantle. *Proceedings of the National Academy of Sciences of the United States of America*, *113*(40), 11,127–11,130. https://doi.org/10.1073/pnas.1605290113

Rost, S., Garnero, E. J., Williams, Q., & Manga, M. (2005). Seismological constraints on a possible plume root at the core-mantle boundary. *Nature*, *435*(7042), 666–669. https://doi.org/10.1038/nature03620

Sinmyo, R., Hirose, K., & Ohishi, Y. (2019). Melting curve of iron to 290 GPa determined in a resistance-heated diamond-anvil cell. *Earth and Planetary Science Letters*, *510*, 45–52. https://doi.org/10.1016/j.epsl.2019.01.006

Stackhouse, S., Stixrude, L., & Karki, B. B. (2015). First-principles calculations of the lattice thermal conductivity of the lower mantle. *Earth and Planetary Science Letters*, *427*, 11–17. https://doi.org/10.1016/j.epsl.2015.06.050

Stixrude, L., de Koker, N., Sun, N., Mookherjee, M., & Karki, B. B. (2009). Thermodynamics of silicate liquids in the deep Earth. *Earth and Planetary Science Letters*, *278*(3–4), 226–232. https://doi.org/10.1016/j.epsl.2008.12.006

Tangeman, J. A., Phillips, B. L., Navrotsky, A., Weber, J. K. R., Hixson, A. D., & Key, T. S. (2001). Vitreous forsterite (Mg2SiO4): Synthesis, structure, and thermochemistry. *Geophysical Research Letters*, *28*(13), 2517–2520. https://doi.org/10.1029/2000GL012222

Tateno, S., Hirose, K., & Ohishi, Y. (2014). Melting experiments on peridotite to lowermost mantle conditions. *Journal of Geophysical Research: Solid Earth*, *119*, 4684–4694. https://doi.org/10.1002/2013JB010616

Wen, L., & Helmberger, D. V. (1998). Ultra-low velocity zones near the core-mantle boundary from broadband PKP precursors. *Science*, *279*(5357), 1701–1703. https://doi.org/10.1126/science.279.5357.1701

Williams, Q., & Garnero, E. J. (1996). Seismic evidence for partial melt at the base of earth's mantle. *Science*, *273*(5281), 1528–1530. https://doi.org/10.1126/science.273.5281.1528

Yu, S., & Garnero, E. J. (2018). Ultralow velocity zone locations: A global assessment. *Geochemistry, Geophysics, Geosystems*, *19*, 396–414. https://doi.org/10.1002/2017GC007281

Yuan, K., & Romanowicz, B. (2017). Seismic evidence for partial melting at the root of major hot spot plumes. *Science*, *357*(6349), 393–397. https://doi.org/10.1126/science.aan0760

References From the Supporting Information

Boehler, R. (2000). High-pressure experiments and the phase diagram of lower mantle and core materials. *Reviews of Geophysics*, *38*(2), 221–245. https://doi.org/10.1029/1998RG000053

Deng, J., & Lee, K. K. M. (2017). Viscosity jump in the lower mantle inferred from melting curves of ferropericlase. *Nature Communications*, *8*(1), 1997. https://doi.org/10.1038/s41467-017-02263-z

Eggert, J. H., Weck, G., Loubeyre, P., & Mezouar, M. (2002). Quantitative structure factor and density measurements of high-pressure fluids in diamond anvil cells by x-ray diffraction: Argon and water. *Physical Review B: Condensed Matter and Materials Physics*, *65*, 1–12.

Mezouar, M., Faure, P., Crichton, W., Rambert, N., Sitaud, B., Bauchau, S., & Blattmann, G. (2002). Multichannel collimator for structural investigation of liquids and amorphous materials at high pressures and temperatures. *Review of Scientific Instruments*, *73*(10), 3570–3574. https://doi.org/10.1063/1.1505104

Ono, S. (2010). The equation of state of B2-type NaCl. In *Journal of Physics: Conference Series* (Vol. 215, p. 012196). Bristol, England: IOP Publishing. http://doi.org/10.1088/1742-6596/215/1/012196

Prakapenka, V. B., Kubo, A., Kuznetsov, A., Laskin, A., Shkurikhin, O., Dera, P., et al. (2008). Advanced flat top laser heating system for high pressure research at GSECARS: Application to the melting behavior of germanium. *High Pressure Research*, *28*(3), 225–235. https://doi.org/10.1080/08957950802050718

Prescher, C., & Prakapenka, V. B. (2015). DIOPTAS: A program for reduction of two-dimensional X-ray diffraction data and data exploration. *High Pressure Research*, *35*(3), 223–230. https://doi.org/10.1080/08957959.2015.1059835

Prescher, C., Prakapenka, V. B., Stefanski, J., Jahn, S., Skinner, L. B., & Wang, Y. (2017). Beyond sixfold coordinated Si in SiO2 glass at ultrahigh pressures. *Proceedings of the National Academy of Sciences of the United States of America*, *114*(38), 10,041–10,046. https://doi.org/10.1073/pnas.1708882114

Shim, S. H. (2017). PeakPo—A python software for x-ray diffraction analysis at high pressure and high temperature, Zenodo.

Weck, G., Garbarino, G., Ninet, S., Spaulding, D., Datchi, F., Loubeyre, P., & Mezouar, M. (2013). Use of a multichannel collimator for structural investigation of low-Z dense liquids in a diamond anvil cell: Validation on fluid H2 up to 5 GPa. *Review of Scientific Instruments*, *84*(6), 063901. https://doi.org/10.1063/1.4807753

Ye, Y., Gu, C., Shim, S. H., Meng, Y., & Prakapenka, V. (2014). The postspinel boundary in pyrolitic compositions determined in the laser-heated diamond anvil cell. *Geophysical Research Letters*, *41*, 3833–3841. https://doi.org/10.1002/2014GL060060